Texture formation in carbonaceous mesophase fibers

J. Yan and A. D. Rey*
Department of Chemical Engineering, McGill University, 3610 University Street, Montreal, Canada PQ H3A 2B2
(Received 2 October 2001; published 21 February 2002)

Carbonaceous mesophases are discotic nematic liquid crystals that are spun into high performance carbon fibers using the melt spinning process. The spinning process produces a wide range of different fiber textures. Planar polar (PP) and planar radial (PR) textures are two ubiquitous ones. This paper presents theory and simulation of the texture formation process using the Landau-de Gennes mesoscopic theory for discotic liquid crystals. The computed PP and PR textures phase diagram, given in terms of temperature and fiber radius, is presented to establish the processing conditions and geometric factors that lead to the selection of these textures. Thin fibers adopt the PR texture, while thicker fibers and higher temperatures adopt the PP texture. The influence of elastic anisotropy to the formation of textures and structure is thoroughly characterized.

DOI: 10.1103/PhysRevE.65.031713 PACS number(s): 61.30.−v

I. INTRODUCTION

Carbonaceous mesophases, such as coal tar and petroleum pitches, are used in the industrial manufacturing of high performance carbon fibers. This relatively new carbon fiber is more competitive than the conventional one made from the acrylic precursors in several application areas [1]. The thermodynamic phase that describes carbonaceous mesophases is the discotic nematic liquid crystal (DNLC) state [2]. Liquid crystals are intermediate (i.e., mesophase) phases, typically found for anisodiametric organic molecules, which exist between the higher temperature isotropic liquid state and the lower temperature crystalline state. Carbonaceous mesophases are composed of disklike molecules. Figure 1 shows the molecular geometry, positional disorder, and uniaxial orientational order of discotic nematic liquid crystals. The partial orientational order of the molecular unit normal $\mathbf{u}$ is along the average orientation or director $\mathbf{n}$ ($\mathbf{n}\cdot\mathbf{n}=1$). The name discotic distinguishes the molecular geometry and the name nematic identifies the type of liquid crystalline orientational order.

The industrial fabrication of mesophase carbon fiber using the conventional melt spinning process typically produces micrometer-sized cylindrical filaments whose cross-sectional area displays a variety of transverse textures [3], that is, different spatial arrangements of the average orientation $\mathbf{n}$ on the plane perpendicular to the fiber axis. The selection mechanisms that drive the texture formation pattern are at present not well understood, but due to the strong structure-properties correlations, they are essential for product optimization [1,3].

A question of fundamental importance to the melt spinning of carbonaceous mesophases is to determine how elastic and viscous mechanisms affects the fiber process-induced structuring and cross-sectional fiber textures's selection. When considering elastic mechanisms, it is necessary to identify the three fundamental elastic modes of these materials. Figure 2 shows the three types of elastic deformations, splay, twist, and bend, and the corresponding modulus K_{11}, K_{22}, and K_{33}, known as Frank elasticity constants [4]. The bulk free energy density is given by

$$f_n=\tfrac{1}{2}K_{11}(\nabla\cdot\mathbf{n})^2+\tfrac{1}{2}K_{22}(\mathbf{n}\cdot\nabla\times\mathbf{n})^2+\tfrac{1}{2}K_{33}|\mathbf{n}\times(\nabla\times\mathbf{n})|^2. \quad (1)$$

Thermodynamic stability requires,

$$K_{11}>0; \quad K_{22}>0; \quad K_{33}>0. \quad (2)$$

In contrast to rodlike nematics, for disclike nematics the bending disc's trajectories give rise to a splay deformation, and the splaying disc's trajectories give rise to a bend deformation; by disc trajectory it means the curve locally orthogonal to the director. For DNLCs, the following inequalities hold [5]:

$$K_{22}>K_{11}; \quad K_{22}>K_{33}, \quad (3)$$

which indicates that planar deformations are favored.

It is known [3,6] that the observed cross-section fiber textures belong to a numbers of families, such as onion, radial, mixed, PAN-AM, to name a few. Figure 3 shows the schematics of two cross-sectional textures most commonly seen in mesophase carbon fibers. The dashed line indicates the trajectories of the molecular planes, Fig. 3(a) shows the pla-

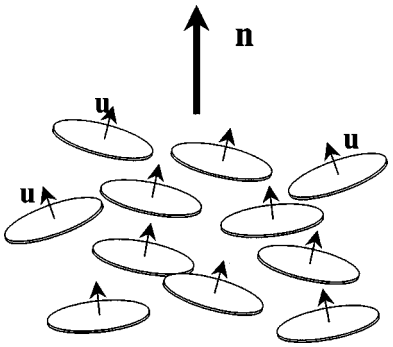

FIG. 1. Definition of director orientation of a uniaxial discotic nematic liquid crystalline material. The director $\mathbf{n}$ is the average orientation of the unit normals to the disklike molecules in a discotic nematic phase.

*Corresponding author. Email address: alejandro.rey@mcgill.ca

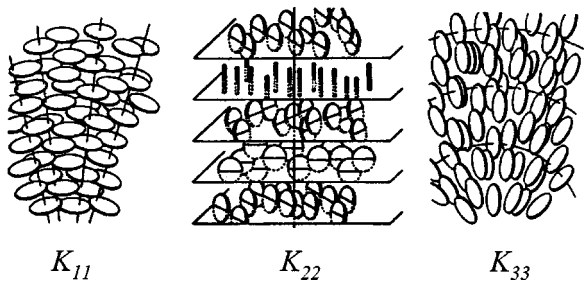

FIG. 2. Schematics of the elastic splay (left), twist (center), and bend (right) deformation for uniaxial discotic nematics. Note that the splay (bend) mode involves bending (splaying) of the disk's trajectories, in contrast to the case of uniaxial rodlike nematics. A disk trajectory is a curve locally orthogonal to the director. Adapted from Ref. [6].

nar radial (PR) texture, in which only the pure bend mode exists with one defect in the center of strength $s=+1$, and Fig. 3(b) shows the planar polar (PP) texture, in which two modes of deformation, splay and bend, exist with two defects of the strength $s=+1/2$. Figures 3(c) and 3(d) are the corresponding director fields's schematics of the PP and PR textures. The defects arise due to the constraints of tangential boundary conditions and a planar two dimensional (2D) orientation field. Defects are singularities in the director field and are characterized by strength (1/2,1, . . .) and sign ($\pm$) [4]. The strength of a disclination determines the amount of orientation distortion and the sign corresponds to the sense (i.e., clockwise or anticlockwise) of orientation rotation while circling the defects. Since the energy of a defect scales with the square of the defect strength [4], the planar polar texture would seem to emerge, so as to minimize the elastic energy associated with orientation distortions. In addition, defects of equal sign repel each other, while defects of different sign attract. As shown below, in the PP texture, defect-defect interaction plays a critical role in the geometry of the texture. For discussions and references on rodlike nematics in cylindrical geometries, see for example [7,8]. The phase diagram of nematic textures in cylindrical geometries as a function of temperature and fiber radius in the absence of elastic anisotropy has been given by Sonnet, Kilian, and Hess [9].

Theory and simulation of liquid crystalline materials continues to be performed using macroscopic, mesoscopic, and molecular models [4]. Macroscopic models based on the Leslie-Ericksen director equations are unsuitable to simulate texture formation because defects are singularities in the orientation field. On the other hand, mesoscopic models based on the second moment of the orientation distribution function is well suited to capture the formation of liquid crystalline textures, because defects are nonsingular solutions to the governing equations. A very well established mesoscopic model in liquid crystalline materials is based on the Landau–de Gennes free energy [4] and is used in this paper.

The objectives of this paper are:

(1) To simulate the transient formation of the PR and PP texture that is commonly observed during the melt spinning of carbonaceous mesophase.

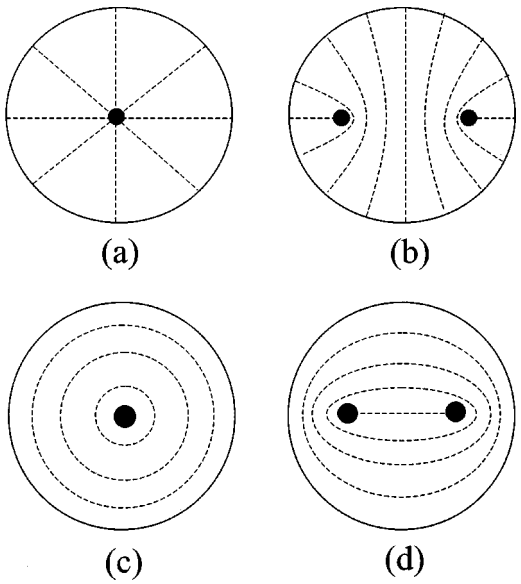

FIG. 3. Schematics of two cross-sectional textures most commonly seen in mesophase carbon fibers. The dashed line indicates the trajectories of the molecular planes, (a) shows the planar radial (PR) texture, in which only the pure bend mode exists with one defect in the center of strength $S=+1$, and (b) shows the planar polar (PP) texture, with splay and bend, and two defects of the strength $S=+1/2$. (c) and (d) are the corresponding director field's schematics of the PP and PR textures. The defects arise due to the constraints of tangential boundary conditions and a planar 2D orientation field.

(2) To characterize the mechanisms of PR and PP texture selection in DNLCs.

(3) To compute a texture phase diagram, given in terms of temperature and fiber radius, and to establish the geometric and operating conditions that lead to the characteristic textures.

(4) To discuss the influence of elastic anisotropy ($K_{11} \neq K_{22} \neq K_{33}$) on the formation of fiber texture.

This paper is organized as follows. Section II presents the theory and the Landau–de Gennes governing equations. Section III discusses the computational methods to solve the model. Section IV shows the numerical solutions of our model, and also, discusses the characteristics of the texture phase diagram and the effect of elastic anisotropy. Finally conclusions are presented.

II. THEORY AND GOVERNING EQUATIONS

In this section, we present the Landau–de Gennes theory for nematic liquid crystals, and the parametric equations used to describe mesophase fiber texture formation. As mentioned above, the theory is well suited to simulate texture formation since defects are nonsingular solutions to the governing equations.

A. Definition of orientation and alignment

The microstructure of DNLCs is characterized by a second-order symmetric and traceless tensor, known generally as tensor order parameter **Q** [10],

$$\mathbf{Q}=S\left(\mathbf{nn}-\frac{1}{3}\mathbf{I}\right)+\frac{1}{3}P(\mathbf{mm}-\mathbf{ll}), \tag{4}$$

where the following restrictions apply:

$$\mathbf{Q}=\mathbf{Q}^T;\quad \mathrm{tr}(\mathbf{Q})=0;\quad -\tfrac{1}{2}\leqslant S\leqslant 1;\quad -\tfrac{3}{2}\leqslant P\leqslant\tfrac{3}{2}, \tag{5}$$

$$\mathbf{n}\cdot\mathbf{n}=\mathbf{m}\cdot\mathbf{m}=\mathbf{l}\cdot\mathbf{l}=\mathbf{1};\quad \mathbf{nn}+\mathbf{mm}+\mathbf{ll}=\mathbf{I}=\begin{bmatrix}1&0&0\\0&1&0\\0&0&1\end{bmatrix}. \tag{6}$$

The uniaxial director **n** corresponds to the maximum eigenvalue $\mu_n=\frac{2}{3}S$, the biaxial director **m** corresponds the second largest eigenvalue $\mu_m=\frac{1}{3}(S-P)$, and the second biaxial director $\mathbf{l}(=\mathbf{n}\times\mathbf{m})$ corresponds to the smallest eigenvalue $\mu_l=-\frac{1}{3}(S+P)$. The orientation is defined completely by the orthogonal director triad (**n**,**m**,**l**). The magnitude of the uniaxial scalar order parameter S is a measure of the molecular alignment along the uniaxial director **n**, and is given as $S=\frac{3}{2}(\mathbf{n}\cdot\mathbf{Q}\cdot\mathbf{n})$. The magnitude of the biaxial scalar order parameter P is a measure of the molecular alignment in a plan perpendicular to the direction of uniaxial director **n**, and is given as $P=\frac{3}{2}(\mathbf{m}\cdot\mathbf{Q}\cdot\mathbf{m}-\mathbf{l}\cdot\mathbf{Q}\cdot\mathbf{l})$. On the principal axes, the tensor order parameter **Q** is represented as

$$\mathbf{Q}=\begin{bmatrix}-\frac{1}{3}(S-P)&0&0\\0&-\frac{1}{3}(S+P)&0\\0&0&\frac{2}{3}S\end{bmatrix}. \tag{7}$$

Both S and P are positive for normal DNLCs. The Landau–de Gennes model uses the tensor order parameter to describe nematic ordering. According to Eq. (7), the model is able to describe biaxial ($S\neq 0$, $P\neq 0$), uniaxial ($S\neq 0$, $P=0$), and isotropic ($S=0$, $P=0$) states.

B. Landau–de Gennes mesoscopic model for liquid crystalline materials

According to the Landau–de Gennes model, the bulk energy density of nematic liquid crystals (NLC) in the absence of external fields is given by [11,12]

$$f_b=f_0+f_s+f_l, \tag{8a}$$

$$f_l=f_{l2}+f_{l3}, \tag{8b}$$

$$f_s=A\mathbf{Q}:\mathbf{Q}+B\mathbf{Q}:(\mathbf{Q}\cdot\mathbf{Q})+C(\mathbf{Q}:\mathbf{Q})^2, \tag{8c}$$

$$f_{l2}=L_1\nabla\mathbf{Q}:(\nabla\mathbf{Q})^T+L_2(\nabla\cdot\mathbf{Q})\cdot(\nabla\cdot\mathbf{Q}), \tag{8d}$$

$$f_{l3}=L_3\mathbf{Q}:(\nabla\mathbf{Q}:\nabla\mathbf{Q})+\cdots, \tag{8e}$$

where $A,B,C,L_1,L_2,L_3,\ldots$ are coefficients of the specified terms. f_0 is the free energy density of the isotropic state. The term is related to the conventional thermodynamic parameters, such as temperature and pressure, and independent to **Q**. f_s is the short-range energy density, which is responsible for the nematic-isotropic phase transition, f_l is the long-range energy, f_{l2} is the second-order long-range free energy density, and f_{l3} is the third-order contribution to the long-range free energy density. By assuming that **Q** is uniaxial and comparing f_{l2} with f_n [Eq. (1)] it is found that $K_{11}=K_{33}$. To remove this restriction f_{l3} must be nonzero. It is known that there are six different third-order expressions. For rodlike nematics it was shown that representative experimental $\{K_{ii}\}$; $(ii=11,22,33)$ data is well captured by retaining only the term $L_3\mathbf{Q}_{\alpha\beta}\mathbf{Q}_{\gamma\delta,\alpha}\mathbf{Q}_{\gamma\delta,\beta}$ in the f_{l3} expression [13]. The same approach will be used in this paper. Using the one parameter Doi model for f_s [14], the dimensionless free energy densities are given by

$$f_s^*=\frac{3}{U}[\tfrac{1}{2}(1-\tfrac{1}{3}U)\mathbf{Q}:\mathbf{Q}-\tfrac{1}{3}U\mathbf{Q}:(\mathbf{Q}\cdot\mathbf{Q})+\tfrac{1}{4}U(\mathbf{Q}:\mathbf{Q})^2], \tag{9a}$$

$$f_{l2}^*=\frac{L_1}{2ckT^*R^2}[\tilde{\nabla}\mathbf{Q}\vdots(\tilde{\nabla}\mathbf{Q})^T]+\frac{L_2}{2ckT^*R^2}(\tilde{\nabla}\cdot\mathbf{Q})\cdot(\tilde{\nabla}\cdot\mathbf{Q}), \tag{9b}$$

$$f_{l3}^*=\frac{L_3}{2ckT^*R^2}[\mathbf{Q}:(\tilde{\nabla}\mathbf{Q}:\tilde{\nabla}\mathbf{Q})], \tag{9c}$$

where U is the nematic potential, which is inversely proportional to the temperature in a thermotropic liquid crystal, and c, k, T^* are the number density of discs, the Boltzmann's constant, and an absolute reference temperature just below the isotropic-nematic phase transition temperature, respectively. Comparing Eq. (1) the Landau coefficients (LC) $\{L_i\}$, $i=1,2,3$ are related to the Frank's constant of uniaxial LCs in the following way [12,15,16]:

$$L_1=\frac{3K_{22}-K_{11}+K_{33}}{6S^2}, \tag{10a}$$

$$L_2=\frac{K_{11}-K_{22}}{S^2}, \tag{10b}$$

$$L_3=\frac{K_{33}-K_{11}}{2S^3}, \tag{10c}$$

$$K_{11}=S^2(2L_1+L_2-\tfrac{2}{3}SL_3), \tag{11a}$$

$$K_{22}=S^2(2L_1-\tfrac{2}{3}SL_3), \tag{11b}$$

$$K_{33}=S^2(2L_1+L_2+\tfrac{4}{3}SL_3). \tag{11c}$$

Using Eqs. (11) and inequalities (2) the following restrictions have to be obeyed under uniaxial ordering:

$$2L_1+L_2-\tfrac{2}{3}SL_3\geqslant 0; \tag{12a}$$

$$2L_1-\tfrac{2}{3}SL_3\geqslant 0; \tag{12b}$$

$$2L_1+L_2+\tfrac{4}{3}SL_3\geqslant 0. \tag{12c}$$

In addition, since twist is the highest elastic constant in DNLCs, the Landau coefficient L_2 is negative [10,17],

$$L_2 < 0. \tag{13}$$

Using the classical gradient flow model, the time-dependent equation in terms of $\mathbf{Q}$ and $\nabla\mathbf{Q}$ is found to be [14]

$$-\gamma(\mathbf{Q})\frac{d\mathbf{Q}}{dt} = \frac{\delta F}{\delta \mathbf{Q}} = \left(\frac{\partial f_b}{\partial \mathbf{Q}} - \nabla\cdot\frac{\partial f_b}{\partial \nabla\mathbf{Q}}\right)^{[s]}, \tag{14}$$

where $[s]$ indicates the symmetric and traceless, $\gamma(\mathbf{Q})$ is the rotational viscosity coefficient, and $\delta F/\delta\mathbf{Q}$ is the functional derivative of the total energy F. Substituting Eq. (9) into Eq. (14) yields the following governing equations of $\mathbf{Q}(\mathbf{x},t)$:

$$\begin{aligned}\frac{d\mathbf{Q}}{dt} = &-6\overline{D_r}\left[\frac{\partial f_b^*}{\partial \mathbf{Q}} - \nabla\cdot\frac{\partial f_b^*}{\partial \nabla\mathbf{Q}}\right]^{[s]} = -6\overline{D_r}\Bigg\{\frac{3}{U}[(1-\tfrac{1}{3}U)\mathbf{Q} \\ &- U(\mathbf{Q}\cdot\mathbf{Q} - \tfrac{1}{3}(\mathbf{Q}:\mathbf{Q})\mathbf{I}) + U(\mathbf{Q}:\mathbf{Q})\mathbf{Q}] \\ &+ \frac{L_3}{2ckT^*}[(\nabla\mathbf{Q}:\nabla\mathbf{Q}) - \tfrac{1}{3}\mathrm{tr}(\nabla\mathbf{Q}:\nabla\mathbf{Q})\mathbf{I}]\Bigg\} \\ &+ 6\overline{D_r}\Bigg(\frac{L_1}{ckT^*}\nabla^2\mathbf{Q} + \frac{L_2}{2ckT^*}\Bigg\{\nabla(\nabla\cdot\mathbf{Q}) + [\nabla(\nabla\cdot\mathbf{Q})]^T \\ &- \frac{2}{3}\mathrm{tr}[\nabla(\nabla\cdot\mathbf{Q})]\mathbf{I}\Bigg\} + \frac{L_3}{ckT^*}[(\nabla\cdot\mathbf{Q})\cdot\nabla\mathbf{Q}] \\ &+ \frac{L_3}{ckT^*}[\mathbf{Q}:(\nabla\nabla\mathbf{Q})]\Bigg),\end{aligned} \tag{15a}$$

$$\overline{D_r} \approx D_r\frac{1}{(1-(3/2)\mathbf{Q}:\mathbf{Q})^2}, \quad D_r = \frac{ckT}{6\eta}, \tag{15b}$$

where $\overline{D_r}$ is the microstructure dependent rotational diffusivity, D_r is the preaveraged rotational diffusivity or isotropic diffusivity, which is independent of $\mathbf{Q}$, and η is a viscosity. The relation between $\overline{D_r}$ and $\gamma(\mathbf{Q})$ can be read off by comparing Eq. (14) and (15a). Nondimensioning Eq. (15) yields

$$\frac{d\mathbf{Q}}{d\tilde{t}} = \mathbf{S} + \mathbf{L}, \tag{16a}$$

$$\begin{aligned}\mathbf{S} = &-\frac{1}{U}\frac{3}{U}[1-\tfrac{3}{2}(\mathbf{Q}:\mathbf{Q})]^{-2} \\ &\times[(1-\tfrac{1}{3}U)\mathbf{Q}\cdot U(\mathbf{Q}\cdot\mathbf{Q} - \tfrac{1}{3}(\mathbf{Q}:\mathbf{Q})\mathbf{I}) \\ &+ U(\mathbf{Q}:\mathbf{Q})\mathbf{Q}],\end{aligned} \tag{16b}$$

$$\begin{aligned}\mathbf{L} = &\frac{\xi^2}{R^2}\frac{1}{U}[1-\tfrac{3}{2}(\mathbf{Q}:\mathbf{Q})]^{-2} \\ &\times\Bigg(\tilde{\nabla}^2\mathbf{Q} + \frac{\tilde{L}_2}{2}\{\tilde{\nabla}(\tilde{\nabla}\cdot\mathbf{Q}) + [\tilde{\nabla}(\tilde{\nabla}\cdot\mathbf{Q})] \\ &- \tfrac{2}{3}\mathrm{tr}[\tilde{\nabla}(\tilde{\nabla}\cdot\mathbf{Q})]\mathbf{I}\} + \tilde{L}_3[(\tilde{\nabla}\cdot\mathbf{Q})\cdot\tilde{\nabla}\mathbf{Q}] \\ &+ \tilde{L}_3[\mathbf{Q}:(\tilde{\nabla}\tilde{\nabla}\mathbf{Q})]\Bigg) - \frac{\xi^2}{R^2}\frac{1}{U}\frac{\tilde{L}_3}{2}[1-\tfrac{3}{2}(\mathbf{Q};\mathbf{Q})]^{-2} \\ &\times[(\tilde{\nabla}\mathbf{Q}:\tilde{\nabla}\mathbf{Q}) - \tfrac{1}{3}\mathrm{tr}(\tilde{\nabla}\mathbf{Q}:\tilde{\nabla}\mathbf{Q})\mathbf{I}],\end{aligned} \tag{16c}$$

where $\tilde{t} = t3ckT^*/\eta$ is dimensionless time, $U = 3T^*/T$ is dimensionless temperature, $\xi = (L_1/ckT^*)^{1/2}$ is molecular length scale, $\tilde{L}_2 = L_2/L_1$ and $\tilde{L}_3 = L_3/L_1$ are ratios of elastic coefficients, and R is geometry length scale (i.e., the fiber radius), $\mathbf{S}$ is the short-range contribution, and $\mathbf{L}$ is the long-range distribution.

The dimensionless parameters of the model are U, $\mathcal{R} = R/\xi$, $\tilde{L}_2$, and $\tilde{L}_3$. The nematic potential U is a dimensionless temperature that controls the equilibrium order parameter S_{eq} at the phase transition. According to the Doi model of the short-range energy, the temperature dependence of S at equilibrium is [14]

$$S_{\mathrm{eq}} = \tfrac{1}{4} + \tfrac{3}{4}\left(1 - \frac{8}{3U}\right)^{1/2}, \tag{17a}$$

$$U = \frac{3T^*}{T}, \tag{17b}$$

where T^* is a reference temperature just below the isotropic-nematic phase transition temperature such as we defined before. For $U < 8/3$ the stable phase is isotropic, for $8/3 \leqslant U \leqslant 3$ there is biphasic equilibrium, and for higher values of U the phase is uniaxial nematic. In this paper, we have used $2.7 \leqslant U \leqslant 6.55$. The parameter $\mathcal{R} = R/\xi$ is the ratio of the fiber radius to the internal length scale ξ. The internal length scale represents the characteristic size of a defect core and is usually much smaller than the system size R. In this paper, we have used $0 < \mathcal{R} < 250$. When $\mathcal{R} \ll 1$, long-range energy dominates, spatial gradients are costly and homogeneous states are selected. On the other hand, when $\mathcal{R} \gg 1$, long-range elasticity is insignificant with respect to short-range elasticity and defects proliferate, since spatially, nonhomogeneous states are energetically not costly. The elastic constants ratios $\tilde{L}_2 = L_2/L_1$ and $\tilde{L}_3 = L_3/L_1$ are two measures of elastic anisotropy. When $\tilde{L}_2, \tilde{L}_3$ are equal to zero, all elastic modes (K_{11}, K_{22}, K_{33}) have the same elastic modulus. To satisfy the thermodynamic restrictions Eqs. (12) and (13), we set $\tilde{L}_2 = -0.5$ throughout and limit the range of $\tilde{L}_3$ to $-1.125 \leqslant S\tilde{L}_3 \leqslant 2.25$. The governing Eq. (16) is solved in the circle $(\tilde{r} = 0.5)$ with the following boundary conditions:

$$t^* > 0, \quad \tilde{r} = 0.5, \quad \mathbf{Q} = \mathbf{Q}_{\mathrm{eq}},$$

$$\mathbf{Q}_{\mathrm{eq}} = S_{\mathrm{eq}}(\boldsymbol{\alpha}\boldsymbol{\alpha} - \tfrac{1}{3}\delta), \tag{18}$$

where $\tilde{r}$ is the dimensionless radial distance ($\tilde{r} = r/R$), and $\tilde{r} = 0$ is the center of the computational domain (i.e., fiber axis). The Dirichlet boundary condition sets the eigenvalues of uniaxial tensor order parameter equal to its equilibrium value ($S = S_{\mathrm{eq}}$), and the distinct eigenvector **n** perpendicular to the azimuthal $\boldsymbol{\alpha}$ direction of the cylindrical coordinates system ($\tilde{r}, \alpha$). The symbol $\boldsymbol{\alpha}$ represents the unit vector along the azimuthal α direction. The initial conditions are

$$t^* = 0, \quad \mathbf{Q}_{\mathrm{ini}} = S_{\mathrm{ini}}(\mathbf{n}_{\mathrm{ini}}\mathbf{n}_{\mathrm{ini}} - \tfrac{1}{3}\delta) + \tfrac{1}{3}P_{\mathrm{ini}}(\mathbf{m}_{\mathrm{ini}}\mathbf{m}_{\mathrm{ini}} - \mathbf{l}_{\mathrm{ini}}\mathbf{l}_{\mathrm{ini}}), \tag{19}$$

where S_{ini} and P_{ini} are infinitesimally small random numbers, and $\mathbf{n}_{\mathrm{ini}}$, $\mathbf{m}_{\mathrm{ini}}$, and $\mathbf{l}_{\mathrm{ini}}$ are corresponding three random eigenvectors. The initial conditions represent an isotropic state ($S = 0$, $P = 0$) with thermal fluctuations in order (S,P) and orientation (**n**,**m**,**l**).

III. COMPUTATIONAL METHODS

The model Eq. (16) is a set of six coupled nonlinear parabolic partial differential equations, solved in the circle, subjected the auxiliary conditions [see Eqs. (18) and (19)]. The equations are solved using Galerkin finite elements with Lagrangean linear basis functions for spatial discretization and a fifth-order Runge-Kutta-Cash-Karp time adaptive method. Convergence and mesh-independence were established in all cases using standard methods. Spatial discretization was judiciously selected taking into account the length scale of our model. As mentioned above, the Landau-de Gennes model for nematic liquid crystals has an external length scale L_e and an internal length scale L_i as follows:

$$L_e = R, \tag{20a}$$

$$L_i = \xi = \left(\frac{L_1}{ckT^*}\right)^{1/2}, \tag{20b}$$

where R is the fiber radius, and where in the length scale obeys $L_e \gg L_i$. If defects are present, the mesh size has to be commensurate with L_i. It should be noted that the external length scale governs the direction's orientation (**n**,**m**,**l**) while the internal length scale governs the scalar order parameter (S,P). In addition, care should be taken to select an appropriate time integration technique to overcome the intrinsic stiffness of the system. The model equations contain an internal time scale τ_i and an external time scale τ_e. The internal time scale governs the evolution of the scalar order parameters (S,P) and is given by

$$\tau_i = \frac{\eta}{ckT^*}. \tag{21}$$

A much longer external time scale τ_e controls the evolution of the directors and is given by

$$\tau_e = \frac{\eta {L_e}^2}{L_1}. \tag{22}$$

The selected adaptive time integration scheme is able to efficiently take into account the stiffness that rises due to the disparity between time scale $\tau_i \ll \tau_e$.

IV. RESULTS AND DISCUSSION

To visualize the fiber textures we use the solution tensor **Q**, and represent the discotic mesophase by a cuboid **C** whose axes are normal to the directors (**n**,**m**,**l**) and sides are proportional to its eigenvalues. Since **Q** has negative eigenvalues, we use $\mathbf{M} = \mathbf{Q} + \frac{1}{3}\mathbf{I}$ instead of **Q**.

A. Representative planar radial and planar polar textures

Figures 4 and 5 show visualizations of representative PP and PR obtained by solving Eqs. (16). Figures 4(a) and 5(a) shows the computed texture phase diagram, given in terms of nematic potential $1/U = T/3T^*$ as a function of dimensionless fiber radius $\mathcal{R} = R/\xi$, with the auxiliary conditions (18) and (19) and $2.7 \leqslant U \leqslant 6.55$, $0 \leqslant \mathcal{R} \leqslant 300$, $\tilde{L}_2 = -0.5$, $\tilde{L}_3 = 0$. The phase diagram identifies the stability of the textures as a function of temperature and fiber radius. Nanofibers favors the PR texture while lower temperature and larger fiber favors the PP texture. The full line indicates the PP and PR texture transition line, defined by critical values of the temperature and fiber size ($1/U_c, \mathcal{R}_c$). For the parameters used here a good fit to the transition line is

$$\frac{-1}{\frac{1}{U} - \frac{3}{8}} = (\mathcal{R} - \mathcal{R}_c)^n; \quad n = 0.65, \quad \mathcal{R}_c = 37. \tag{23}$$

For large U, the transition is effected by $\mathcal{R}$ (long range), and for large $\mathcal{R}$, the transition is effected by U (short range). At large U the long-range effects at the transition include changes of director distortions and biaxiality. At large $\mathcal{R}$ the short range effects on the transition include changes in the scalar order parameter and defect core size. The dots on the diagrams represent the parametric conditions applied in obtaining the solution shown in Figs. 4(b) and 5(b). For $U < 8/3$, the fiber is isotropic.

Figure 4(b) is a representative typical steady state visualization of **M** corresponding to the PP texture for $U = 6.55$, $\mathcal{R} = 67$, $\tilde{L}_2 = -0.5$, $\tilde{L}_3 = 0$. It clearly shows the molecular orientation of planar polar texture, with the two $s = +1/2$ defects collinear with the fiber axis. The orientation of the defect-defect axis is arbitrary since the system evolves from an isotropic state that contains no texture information. The simulations show the bending distortions close to the two defects and an aligned region between the two defects. Figures 4(c), and 4(d) shows a gray-scale plot and a surface plot of the uniaxial scalar order parameter S as a function of dimensionless position (x^*, y^*). In the gray-scale plot a low order parameter ($S \approx 0$) is black and high order parameter ($S \approx 1$) is white. The dark dots in the figure correspond to the two $s = +1/2$ defects. The narrow peaks in the surface plots indicate the difference in scale between defect cores and fiber radius. At the core of defect S is small, as expected. Figures 4(e) and 4(f) show the corresponding gray-scale and

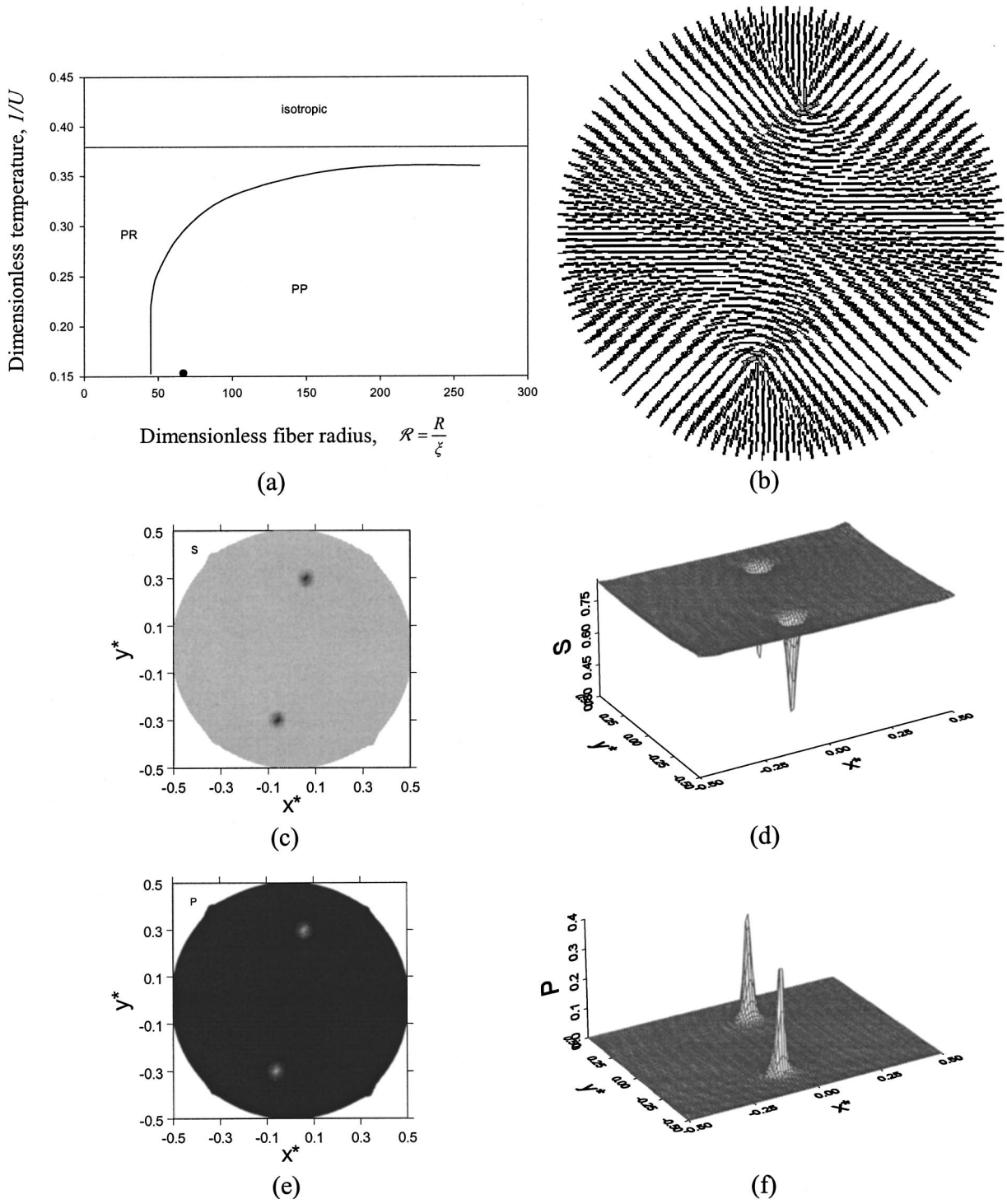

FIG. 4. (a) Computed texture phase diagram, given in terms of nematic potential $1/U=T/3T^*$ as a function of dimensionless fiber radius $\mathcal{R}=R/\xi$, with the auxiliary conditions (18) and (19) and $2.7\leqslant U\leqslant 6.55$, $0\leqslant\mathcal{R}\leqslant 300$, $\tilde{L}_2=-0.5$, $\tilde{L}_3=0$. The full line indicates the PP and PR texture transition line, defined by critical values of the temperature and fiber size $(1/U_c,\mathcal{R}_c)$. The dot on the diagrams represents the parametric conditions applied in obtaining the solution shown in (b). (b) Representative steady state visualization of M corresponding to the PP texture for $U=6.55$, $\mathcal{R}=67$, $\tilde{L}_2=-0.5$, $\tilde{L}_3=0$. (c),(d) Gray-scale plot and a surface plot of the uniaxial scalar order parameter S as a function of dimensionless position (x^*,y^*). In the gray-scale plot a low order parameter ($S\approx 0$) is black and high order parameter ($S\approx 1$) is white. (e),(f) Gray scale and surface plots of the biaxial order parameters P as a function of dimensionless position (x^*,y^*). In the gray-scale plot, $P\approx 0$ corresponds to black and $P\approx 1$ to white.

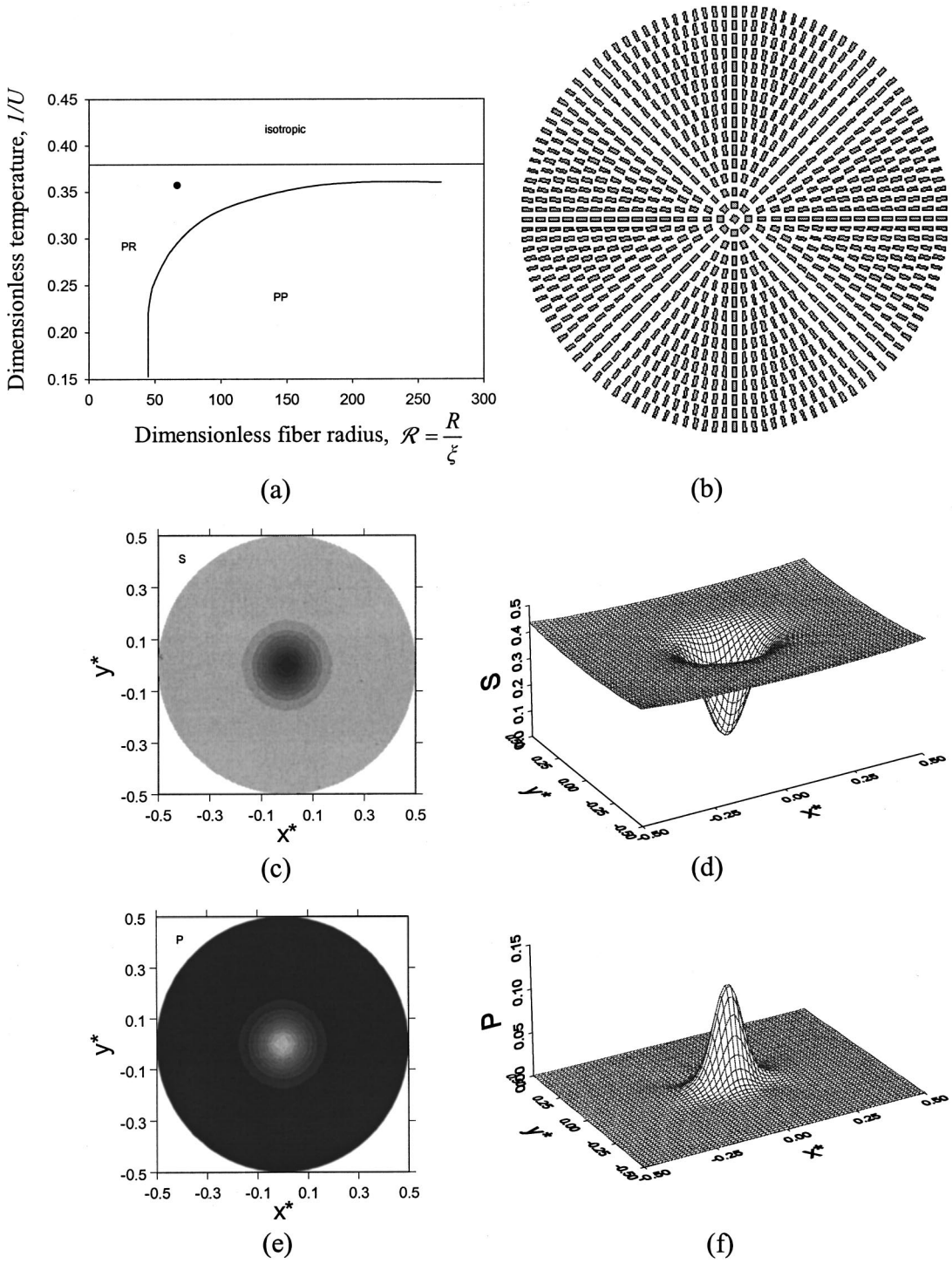

FIG. 5. (a) Computed texture phase diagram, given in terms of nematic potential $1/U = T/3T^*$ as a function of dimensionless fiber radius $\mathcal{R} = R/\xi$, with the auxiliary conditions (18) and (19) and $2.7 \leqslant U \leqslant 6.55$, $0 \leqslant \mathcal{R} \leqslant 300$, $\tilde{L}_2 = -0.5$, $\tilde{L}_3 = 0$. The full line indicates the PP and PR texture transition line, defined by critical values of the temperature and fiber size $(1/U_c, \mathcal{R}_c)$. The dot on the diagrams represents the parametric conditions applied in obtaining the solution shown in (b). (b) Representative steady state visualization of tensor order parameter **M** corresponding to the PR texture for $U = 2.80$, $\mathcal{R} = 67$, $\tilde{L}_2 = -0.5$, $\tilde{L}_3 = 0$. (c),(d) Gray-scale plot and a surface plot of the uniaxial scalar order parameter S as a function of dimensionless position (x^*, y^*). In the gray-scale plot a low order parameter $(S \approx 0)$ is black and high order parameter $(S \approx 1)$ is white. (e),(f) Gray-scale and surface plots of the biaxial order parameters P as a function of dimensionless position (x^*, y^*). In the gray-scale plot, $P \approx 0$ corresponds to black and $P \approx 1$ to white.

surface plots of the biaxial order parameters P as a function of dimensionless position (x^*,y^*). In the gray-scale plot, $P\approx 0$ corresponds to black and $P\approx 1$ to white. The figure clearly shows the biaxial eigenvalues of **Q** at the two defect cores. The corresponding surface plot shows that at the defects core $P\approx 0.4$. Far from the disclination the state is uniaxial. Biaxiality arises because it reduces long range elasticity. Figure 5(b) shows a representative typical steady state visualization of the tensor order parameter **M** corresponding to the PR texture for $U=2.80$, $\mathcal{R}=67$, $\tilde{L}_2=-0.5$, $\tilde{L}_3=0$. There is only one defect in the center, with the strength $s=+1$. The only deformation mode exist in PR texture is bend (K_{33}), because the average molecular trajectories shown on the visualization denote splay. Figures 5(c) and 5(d) shows a gray-scale plot and a surface plot S as a function of dimensionless position (x^*,y^*). It is shown that in the center of the fiber S is small. Figures 5(e)–5(f) show that P increases at the center of fiber. At the disclination center the state is almost negatively uniaxial, and the core is biaxial. Far from the disclination the state is uniaxial.

B. Effect of twist-driven anisotropy on fiber texture selection

In this section we set $\tilde{L}_3=0$ and characterize the effect of $\tilde{L}_2$ on fiber texture selection. The magnitude of $\tilde{L}_2$ determines the difference between twist mode (K_{22}) and the equivalent splay-bend modes $(K_{11}=K_{33})$. The thermodynamically consistent range of $\tilde{L}_2$ is found from Eqs. (12) and (13). To characterize the role of twist elastic anisotropy on texture selection mechanisms the following dimensionless total energy F^* per unit length is analyzed,

$$F^*=\frac{F}{ckT^*}A^*=\int_{A^*}(f_s^*+f_t^*)dA^*, \tag{24}$$

where A^* is the area of the computational domain (circle: $r^*=0.5$), F is the total energy density. Figure 6 shows the dimensionless short-range energy (top), long-range energy (middle) and total energy (bottom) as a function of dimensionless fiber radius $\mathcal{R}$, for $U=3.05$, $\tilde{L}_2=0$ (left column) and $U=3.05$, $\tilde{L}_2=-0.5$ (right column). The discontinuity at $\mathcal{R}=\mathcal{R}_c$ corresponds to the texture PP$\Leftrightarrow$PR transition. Since we perform transient simulations only stable solutions are captured. The left branch of each plot corresponds to the PR texture, and the right bottom branch corresponds to the PP texture. The main effect of decreasing $\tilde{L}_2$ is an horizontal shift of the energy profiles towards smaller $\mathcal{R}$ values and hence $\mathcal{R}_c(\tilde{L}_2=0)>\mathcal{R}_c(\tilde{L}_2=-0.5)$. Increasing $\mathcal{R}$ decreases short- and long-range energy in the PR textures, but only long range in the PP textures. The rate of these changes increases with decreasing $\tilde{L}_2$.

Figure 7 shows the corresponding texture phase diagram for $\tilde{L}_2=0$ and $\tilde{L}_2=-0.5$. The phase transition line of $\tilde{L}_2=-0.5$ shifts left and up in comparison to the $\tilde{L}_2=0$ case. The figure shows that significant influence of $\tilde{L}_2$ on the texture transition only exists for intermediate values of U and $\mathcal{R}$. At low $\mathcal{R}$ the transition line diverges and is independent of U (i.e., vertical line). Since at low $\mathcal{R}$ the transition is sensitive to long-range elasticity, and the main difference in the PR and PP textures is the difference between splay and bend deformations, no significant effect is detected because $\tilde{L}_2$ does not introduce splay-bend anisotropy. On the other hand, at high $\mathcal{R}$ the transition line asymptotes to nematic-isotropic transition line and the texture transition is independent of long range in general, including the $\tilde{L}_2$ contribution.

Figure 8 shows the influence of $\tilde{L}_2$ on the defect core structure for the PR and PP textures, in terms of the three eigenvalues of **Q** as a function of distance. The PR has azimuthal symmetry in the orientation field and the PP has mirror symmetry with respect to the line connecting the two $s=+1/2$ defects. Thus for the PR we show the eigenvalues along the radial direction while for the PP texture we show the eigenvalues as a function of dimensionless distance b^* along a line that is perpendicular to the line connecting the two $s=+1/2$ defects and goes through one of the two equivalent defects. Figures 8(a) and 8(b) show the three eigenvalues of the tensor order parameter **Q** as a function of dimensionless distance b^* for $U=6.55$, $\mathcal{R}=67$, $\tilde{L}_3=0.0$, $\tilde{L}_2=0.0$ (a), and $U=6.55$, $\mathcal{R}=67$, $\tilde{L}_3=0.0$, $\tilde{L}_2=-0.5$ (b), corresponding to the PP textures. In both cases the state at defect center is uniaxial with $\mu_n=\mu_m>0$, $\mu_1<0$. The main effect of L_2 is the decrease in defect core size. Figures 8(b)–8(d) show the three eigenvalues of the tensor order parameter **Q** as a function of dimensionless radial distance r^* for $U=2.8$, $\mathcal{R}=67$, $\tilde{L}_2=0.0$, $\tilde{L}_3=0.0$ (b), and $U=2.8$, $\mathcal{R}=67$, $\tilde{L}_2=-0.5$, $\tilde{L}_3=0.0$ (d), corresponding to the PR textures. In both cases the state at defect center is uniaxial with $\mu_n=\mu_m>0$, $\mu_1<0$. The main effect of L_2 is the decrease in defect core size. To analyze the computed defect core features, the long-range and short-range energies given in Eqs. (8) are expressed in terms of eigenvalues and eigenvectors. For brevity we only discuss the following expression for the PR texture:

$$f_s=-3\mathbf{B}\mu_n\mu_m(\mu_n+\mu_m)+2A(\mu_n^2+\mu_n\mu_m+\mu_m^2)+4C(\mu_n^2+\mu_n\mu_m+\mu_m^2)^2, \tag{25a}$$

$$f_l=\frac{L_1}{2}\left[\mu_{n,r}^2+\mu_{m,r}^2+(\mu_{n,r}+\mu_{m,r})^2+\frac{2(\mu_n-\mu_m)}{r^2}\right]+\frac{L_2}{2}\left[\mu_{n,r}+\frac{(\mu_n-\mu_m)}{r}\right]^2, \tag{25b}$$

where μ_i $(i=m,n)$ are two independent eigenvalues of the tensor **Q**, and $\mu_{i,r}=\partial\mu_i/\partial r$ $(i=m,n)$. At the defect center the state is uniaxial [9], with $\mu_n=\mu_m>0$, $\mu_1<0$, since otherwise the long range energy diverges. In addition the common term between L_1 and L_2

$$\left(L_1+\frac{L_2}{2}\right)\left[\mu_{n,r}+\frac{(\mu_n-\mu_m)}{r}\right]^2 \tag{26}$$

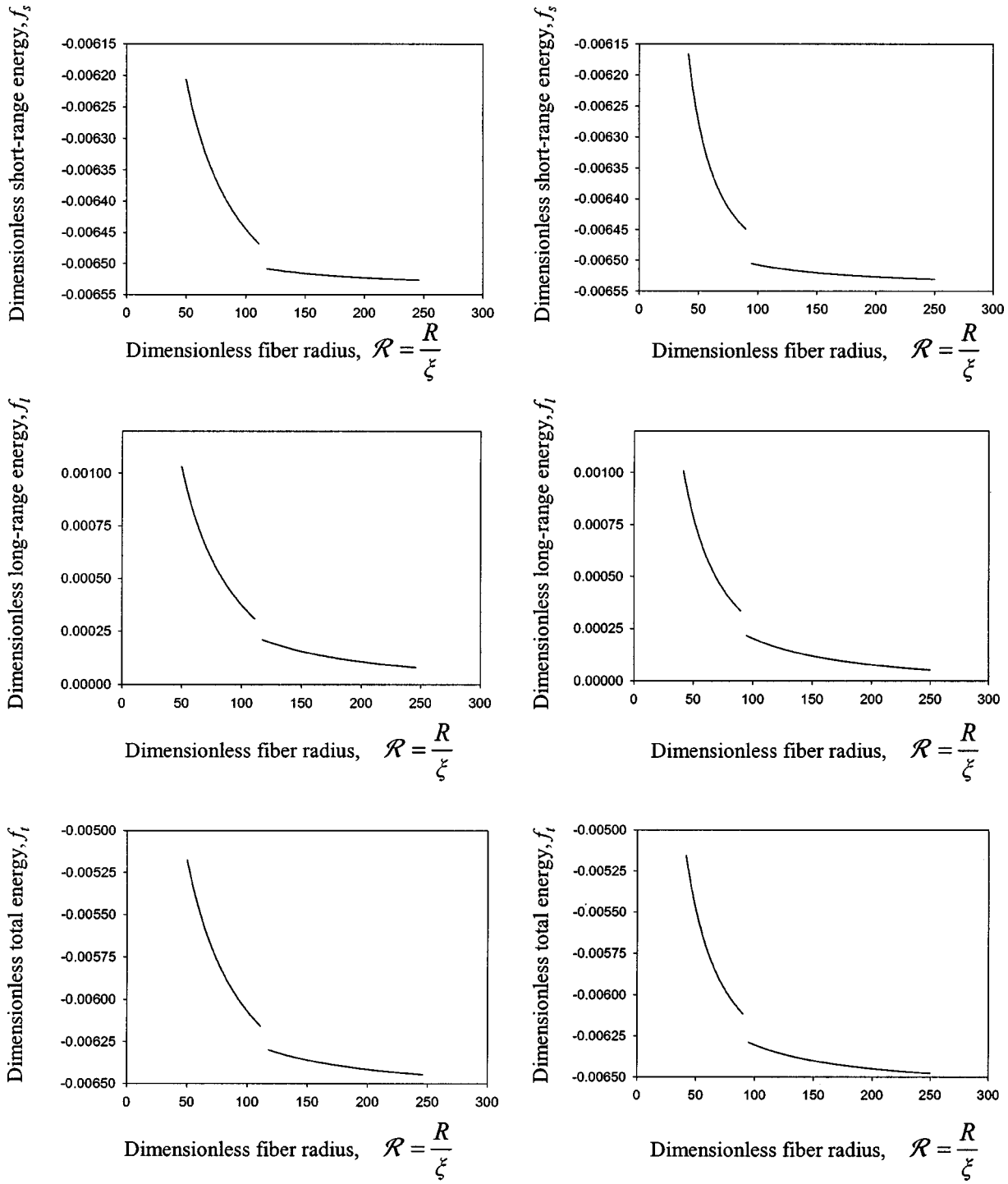

FIG. 6. Dimensionless short-range energy (top), long-range energy (middle), and total energy (bottom) as a function of dimensionless fiber radius $\mathcal{R}$, for $U=3.05$, $\tilde{L}_2=0$ (left column) and $U=3.05$, $\tilde{L}_2=-0.5$ (right column). The discontinuity at $\mathcal{R}=\mathcal{R}_c$ corresponds to the texture PP⇔PR transition.

shows that when L_2 is negative sharper gradients and smaller defect core sizes can be accommodated, as observed when comparing Figs. 8(b) and 8(c).

C. Effect of splay-bend anisotropy on fiber texture selection

In this section we characterize the effect of splay-bend elastic anisotropy, using $\tilde{L}_2=-0.5$ and $\tilde{L}_3\neq 0$. Figure 9 shows the texture phase diagram in terms of $1/U$ and $\mathcal{R}$, for three values of $\tilde{L}_3$. The figure shows that as $|\tilde{L}_3|$ increases the texture transition line shifts up and left in the phase diagram. The texture transition lines retain the same features regardless of the value of $|\tilde{L}_3|$, such that at lower $\mathcal{R}$ the transition lines diverges and at high $\mathcal{R}$ the transition line asymptotes towards the nematic-isotropic transition line. As

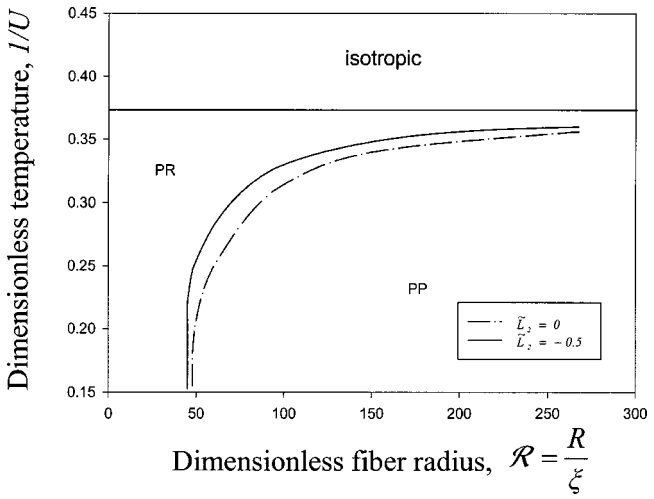

FIG. 7. Computed texture phase diagram, given in terms of nematic potential $1/U=T/3T^*$ as a function of dimensionless fiber radius $\mathcal{R}=R/\xi$, with the auxiliary conditions (18) and (19) and $2.7\leqslant U\leqslant 6.55$, $0\leqslant\mathcal{R}\leqslant 300$, $\tilde{L}_3=0$, $\tilde{L}_2=0$, and $\tilde{L}_2=-0.5$. The phase transition line of $\tilde{L}_2=-0.5$ shifts left and up in comparison to the $\tilde{L}_2=0$ case. The figure shows that significant influence of $\tilde{L}_2$ on the texture transition only exists for intermediate values of U and $\mathcal{R}$.

before, at high $\mathcal{R}$ long range is insignificant and hence the transition lines coalesce. On the other hand, at low $\mathcal{R}$ the figure shows that the diverging transition lines do not coalesce and the effect of $\tilde{L}_3$ persists. The reason is that planar uniaxial textures are sensitive to the splay-bend anisotropy that is created when $\tilde{L}_3\neq 0$.

D. Effect of splay-bend anisotropy on planar polar textures

The geometry of the PP textures is defined by the defect separation distance d. Using simple arguments and the Frank energy of uniaxial NLCs [see Eq. (1)] we can establish the dependence of defect separation distance d as a function of splay-bend anisotropy $d=d(K_{11}-K_{33})$ for certain limiting conditions of the vector model, which is then be tested by the numerical solutions to tensor model [Eqs. (16)]. In this texture the director is tangential to the boundary.

1. Predictions of the vector model

The effect of splay-bend anisotropy on isolated wedge disclination has been characterized [18]. The free energy density f_n around a defect may be written as [18]

$$f_n=\frac{K}{2}\,\frac{\varphi_a^2[1+\varepsilon\cos 2(\varphi-\alpha)]}{r^2}, \tag{27}$$

where φ,α are the orientation angle and the polar angle at a point in polar cylindrical coordinates, $\varphi_\alpha=\partial\varphi/\partial\alpha$, $K=\frac{1}{2}(K_{11}+K_{33})$, and $\varepsilon=(K_{11}-K_{33})/(K_{11}+K_{33})$ is the elastic anisotropy. Minimization of f_n leads to

$$\varphi_{aa}=-\varepsilon[\varphi_{aa}\cos 2(\varphi-\alpha)+\varphi_\alpha(2-\varphi_\alpha)\sin 2(\varphi-\alpha)], \tag{28}$$

where $\varphi_{\alpha\alpha}=\partial^2\varphi/\partial\alpha^2$. Analytical limiting defect solutions to Eq. (28) for wedge $s=+1/2$, $+1$ disclinations can then be used to estimate $d(\varepsilon)$.

(i) Negligible bend: $K_{33}\to 0$, $\varepsilon\to+1$. A solution where the director field trajectories are all circles or parallel lines around the $s=+1/2$ defect is

$$-\frac{\pi}{2}<\alpha<\frac{\pi}{2},\quad \varphi=0\quad\text{and}\quad \frac{\pi}{2}<\alpha<\frac{3\pi}{2},\quad \varphi=\alpha-\frac{\pi}{2} \tag{29}$$

and a pair of these solutions cannot satisfy the boundary conditions. On the other hand, the $s=+1$ solution: $0<\alpha<2\pi$, $\varphi=\alpha+\pi/2$, satisfies the boundary conditions and hence in a DNLC fiber geometry this $s=+1$ solution corresponds to the PR texture and the defect separation distance is $d(\varepsilon=+1)=0$.

(ii) Splay-bend isotropy: $K_{11}=K_{33}$, $\varepsilon=0$. Sufficient increase of ε produces the decay of the $s=+1$ defect into two $s=+1/2$ defects, since some bend is replaced by splay. The location of the defects can be found by using the known boundary conditions and performing a disclination force balance between the two $s=+1/2$ defects and the two images lying outside the fiber [4]. If l is the distance between each $s=+1/2$ defect and its image, then to satisfy the director boundary conditions at $r=R$, the distance x between each defect and the fiber center is

$$xR=l^2. \tag{30}$$

In addition a force balance between each defect and the images gives

$$\frac{1}{2x}=\frac{1}{l+x}+\frac{1}{l+x}, \tag{31}$$

which gives the following defect-defect distance $d=2x$:

$$d^*=\frac{d}{2R}=\frac{1}{\sqrt[4]{5}}. \tag{32}$$

(iii) Negligible splay: $K_{11}\to 0$, $\varepsilon\to-1$. A defect $s=+1/2$ solution consists of straight lines director field trajectories

$$-\frac{\pi}{2}<\alpha<\frac{\pi}{2},\quad \varphi=\alpha\quad\text{and}\quad \frac{\pi}{2}<\alpha<\frac{3\pi}{2},\quad \varphi=\frac{\pi}{2}. \tag{33}$$

A pair of such solutions can only satisfy the boundary conditions at two points when the defects lie next to the fiber rim. Thus some bending is necessary. In addition to minimize the necessary bending to join straight lines the defects should be as far as possible. In a DNLC fiber geometry the solution that best avoids bending corresponds to the PP texture and $d(\varepsilon\to-1)=R-r_c$. In summary, the inequalities driven by splay-bend elastic anisotropy are

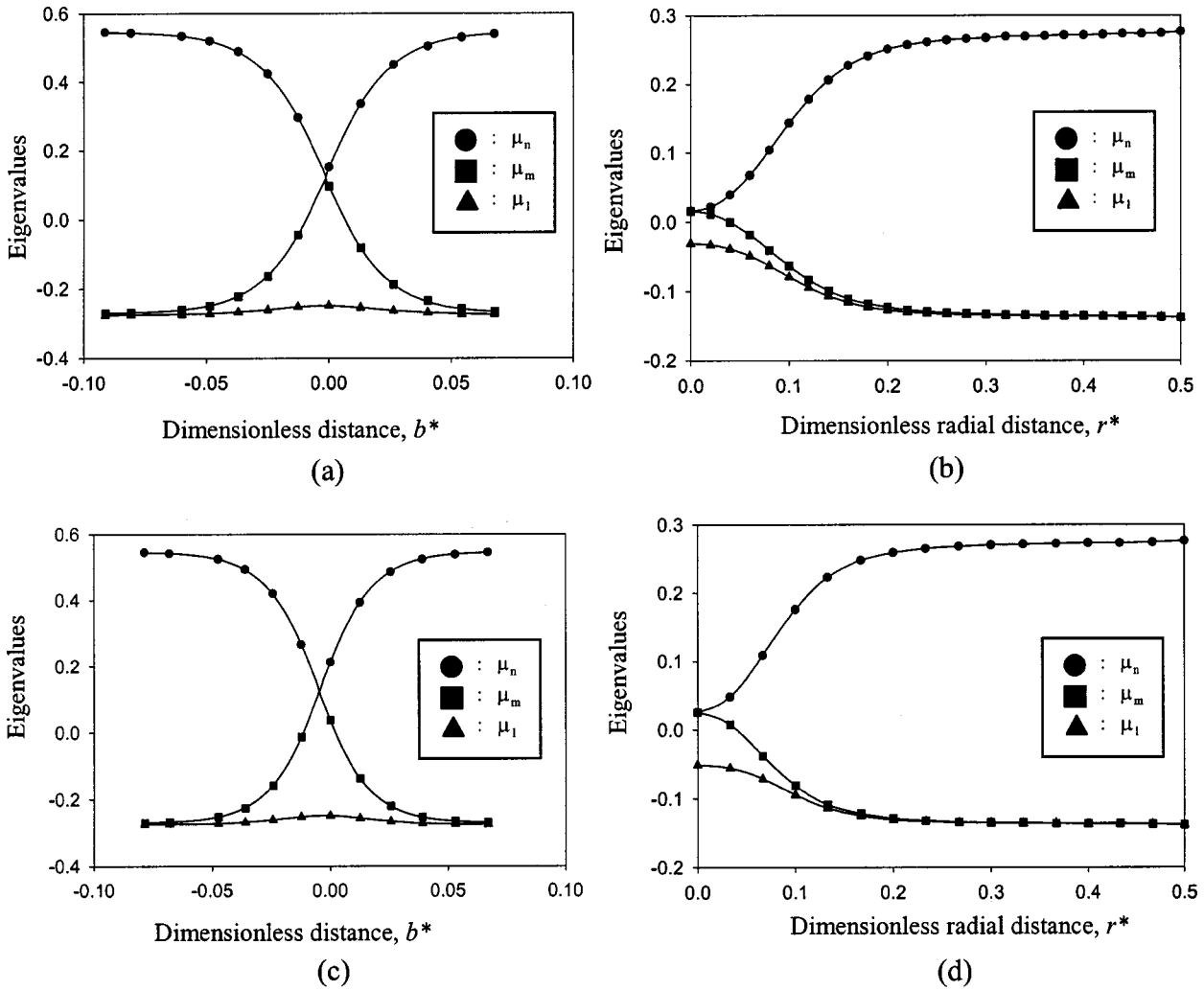

FIG. 8. Eigenvalues of the tensor order parameter **Q** as a function of dimensionless distance b^* for $U=6.55$, $\mathcal{R}=67$, $\tilde{L}_3=0.0$, $\tilde{L}_2=0.0$ (a), and $U=6.55$, $\mathcal{R}=67$, $\tilde{L}_3=0.0$, $\tilde{L}_2=-0.5$ (b), corresponding to the PP textures. In both cases the state at defect center is uniaxial with $\mu_n=\mu_m>0$, $\mu_1<0$. The main effect of L_2 is the decrease in defect core size. (b)–(d) show the three eigenvalues of the tensor order parameter **Q** as a function of dimensionless radial distance r^* for $U=2.8$, $\mathcal{R}=67$, $\tilde{L}_2=0.0$, $\tilde{L}_3=0.0$ (b), and $U=2.8$, $\mathcal{R}=67$, $\tilde{L}_2=-0.5$, $\tilde{L}_3=0.0$ (d), corresponding to the PR textures.

$$d^*(\varepsilon\rightarrow -1)=1>d^*(\varepsilon=0)=\frac{1}{\sqrt[4]{5}}\,\delta^*(\varepsilon=+1)=0. \tag{34}$$

Splay avoidance leads to the PR texture and bend avoidance to the PP textures. The vector model cannot predict the elastic-anisotropy driven texture transitions because the defect reaction $s=+1\leftrightarrow 2s=+1/2$ takes place.

2. Numerical solutions to the tensor model

As mentioned above $\tilde{L}_3$ defines the $K_{11}-K_{33}$ difference,

$$K_{11}-K_{33}=-2L_3S^3. \tag{35}$$

When $\tilde{L}_3<\tilde{L}_{3c}$, $K_{11}>(1+c^2)K_{33}$, the system will avoid the splay mode, and the preferred fiber texture is PR; c denotes a constant. On the other hand, when $\tilde{L}_3>\tilde{L}_{3c}$, $K_{11}>(1+c^2)K_{33}$, the system will try to avoid the bend mode, and the prefered fiber texture is PP with two defects on the rim collinear with the fiber axis.

Figure 10 shows the dimensionless defect distance d^* as a function of $\tilde{L}_3$ for $\mathcal{R}=67$, $\tilde{L}_2=-0.5$, and $U=6.55$ (top), 5.55 (middle), and 4.55 (bottom). The dots for $\tilde{L}_3<\tilde{L}_{3c}$ correspond to the PR texture and the full line corresponds to the PP texture. Note that in Fig. 10 the minimum value of $\tilde{L}_3$ is set by the thermodynamic stability restriction $-1.125\leqslant S\tilde{L}_3$. The horizontal line indicates the case of $\tilde{L}_3=0$, when $d^*=1/\sqrt[4]{5}$ [19,20]. The numerical solutions confirm the theoretical result for all values of U. The computations confirm the expected inequalities (34). When $\tilde{L}_3$ increases, the distance of two defects also increases and eventually asymptotes to the edge of the fiber. Since the boundary conditions are fixed the location of defects cannot be right on the edge. The critical value of $\tilde{L}_3=\tilde{L}_{3c}\approx -1.2$ and is within our com-

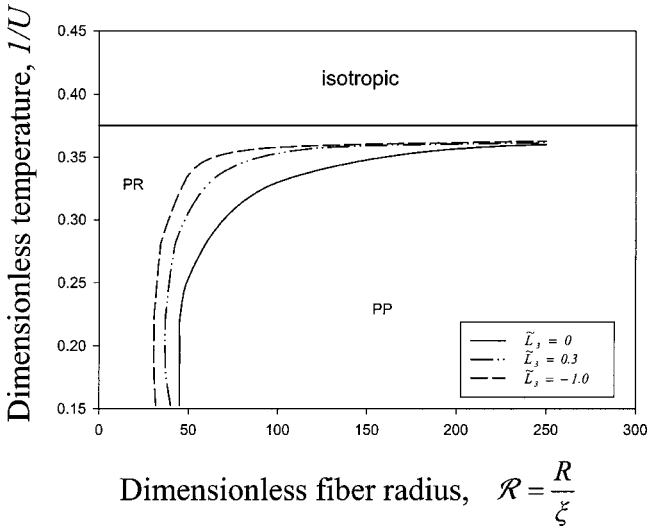

FIG. 9. Computed texture phase diagram, given in terms of nematic potential $1/U = T/3T^*$ as a function of dimensionless fiber radius $\mathcal{R} = R/\xi$, with the auxiliary conditions (18) and (19) and $2.7 \leqslant U \leqslant 6.55$, $0 \leqslant \mathcal{R} \leqslant 300$, $\tilde{L}_2 = -0.5$. For three values of $\tilde{L}_3$, the figure shows that as $|\tilde{L}_3|$ increases the texture transition line shifts up and left in the phase diagram.

putational scheme nearly independent of U. In terms of the vector model, using $S = 0.8$, the critical splay-bend anisotropy is $\varepsilon = -0.75$.

Figure 11(a) shows the visualization of the **M** tensor order parameter for $\tilde{L}_3 < 0$ ($U = 6.55$, $\mathcal{R} = 67$, $\tilde{L}_2 = -0.5$, $\tilde{L}_3 = -1.3$), corresponding to the PR texture with only bend present. Figure 11(b) shows the visualization of the **M** tensor order parameter for $\tilde{L}_3 > 0$ ($U = 6.55$, $\mathcal{R} = 67$, $\tilde{L}_2 = -0.5$, $\tilde{L}_3 = 1.5$) corresponding to the PP texture with an aligned center region and strong splay next to the $s = +1/2$ defects, now located next to the fiber rim.

In contrast to the texture transitions driven by $(U, \mathcal{R})$ discussed above, the transition here is driven by splay-bend elastic anisotropy ($\tilde{L}_3 \neq 0$). Figure 12 shows the second order long-range energy $[f_{2l}(\nabla \mathbf{Q})]$ profile in terms of $\tilde{L}_3$ with the same parametric conditions of Fig. 10. The dots correspond to PR and the curve to the PP texture. The dramatic change of long-range energy at $\tilde{L}_3 = -1.2$ corresponds to the texture transition point due to splay-bend elastic anisotropy. The minimum long-range energy happens when $\tilde{L}_3$ is close to 0.

V. CONCLUSIONS

A model to describe the texture formation in mesophase carbon fibers has been developed, implemented, and shown to replicate commonly observed cross-sectional carbon fiber textures of industrial relevance. The model is based on the classical Landau–de Gennes theory for liquid crystals and has been adapted to describe discotic carbonaceous mesophases. The model is able to predict the formation of planar radial and planar polar textures. The parametric conditions of their stability in terms of temperature and fiber radius have been

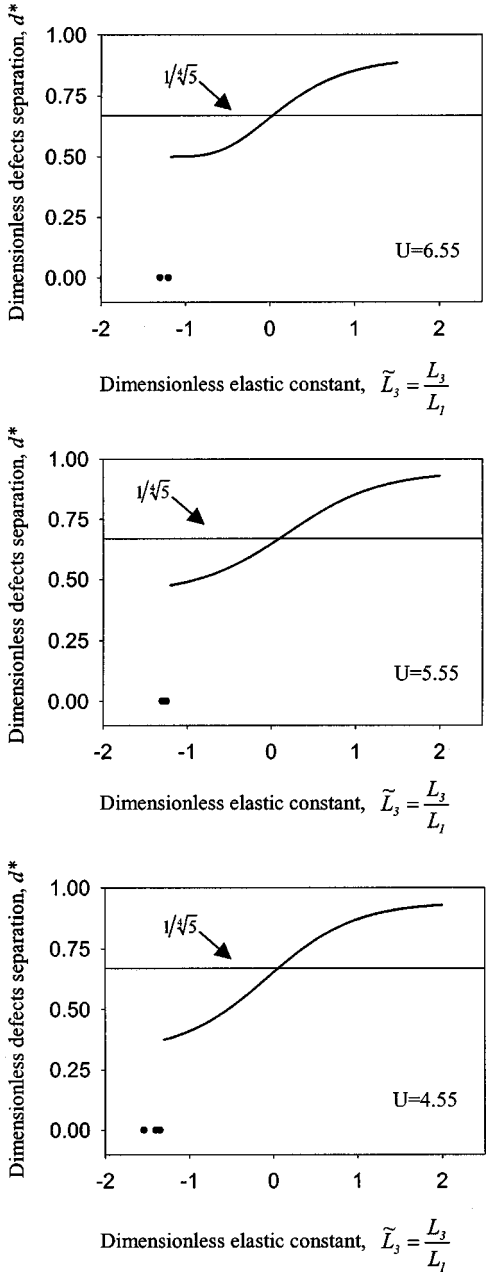

FIG. 10. Dimensionless defect distance d^* as a function of $\tilde{L}_3$ for $\mathcal{R} = 67$, $\tilde{L}_2 = -0.5$, and $U = 6.55$ (top), 5.55 (middle), and 4.55 (bottom). The dots for $\tilde{L}_3 < \tilde{L}_{3c}$ correspond to the PR texture and the full line corresponds to the PP texture. Note that in the figure the minimum value of $\tilde{L}_3$ is set by the thermodynamic stability restriction $-1.125 \leqslant S\tilde{L}_3$. The horizontal line indicates the case of $\tilde{L}_3 = 0$, when $d^* = 1/4\sqrt{5}$ [19]. The numerical solutions confirm the theoretical result for all values of U. The computations confirm the expected inequalities (33). When $\tilde{L}_3$ increases, the distance of two defects also increases and eventually asymptotes to the edge of the fiber. Since the boundary conditions are fixed, the defects' location cannot be right on the edge. The critical value of $\tilde{L}_3 = \tilde{L}_{3c} \approx -1.2$ and is within our computational scheme nearly independent of U. In terms of the vector model, using $S = 0.8$, the critical splay-bend anisotropy is $\varepsilon = -0.75$.

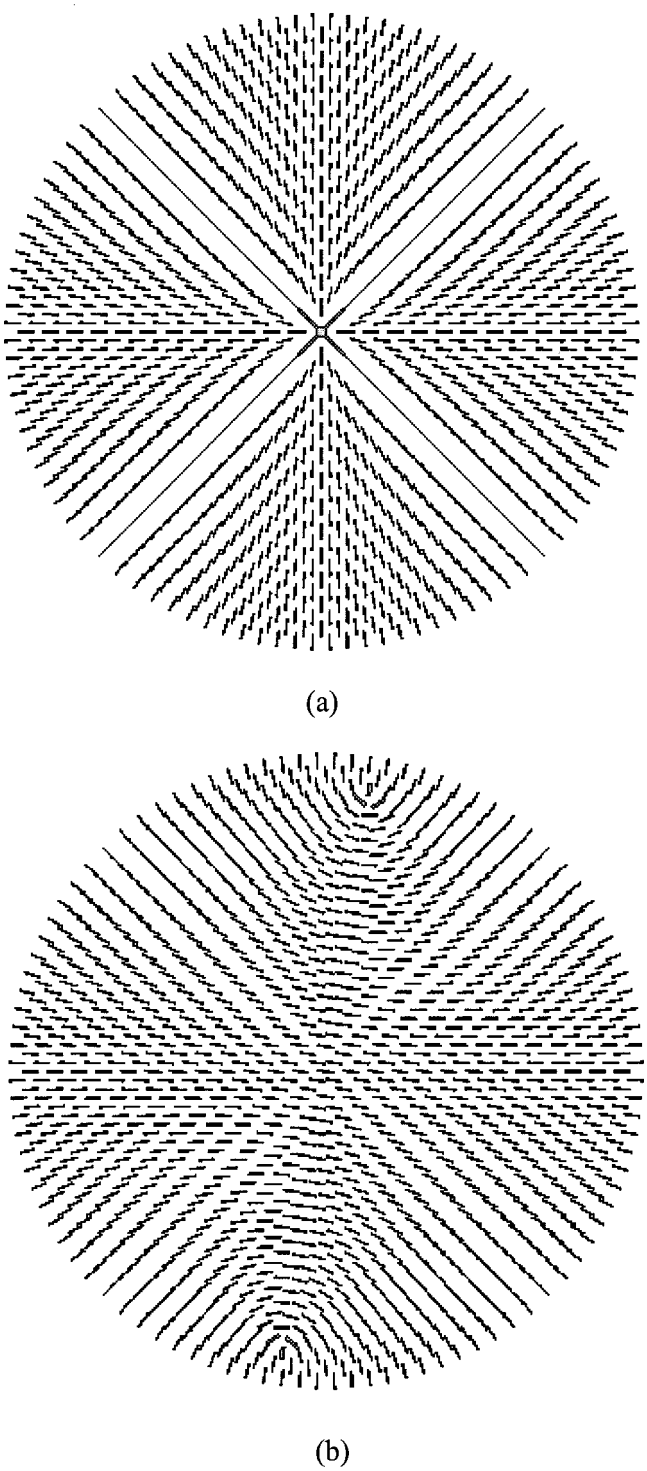

FIG. 11. (a) Computed visualization of the **M** tensor order parameter for $\tilde{L}_3<0$ ($U=6.55$, $\mathcal{R}=67$, $\tilde{L}_2=-0.5$, $\tilde{L}_3=-1.3$), corresponding to the PR texture with only bend present. (b) Computed visualization of the **M** tensor order parameter for $\tilde{L}_3>0$ ($U=6.55$, $\mathcal{R}=67$, $\tilde{L}_2=-0.5$, $\tilde{L}_3=1.5$) corresponding to the PP texture with an aligned center region and strong splay next to the $s=+1/2$ defects, now located next to the fiber rim.

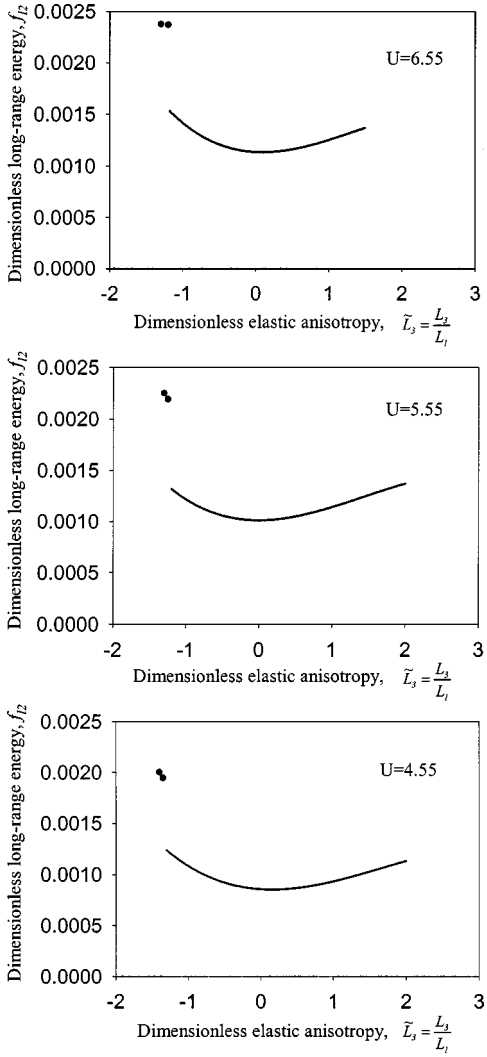

FIG. 12. Second-order long-range energy $[f_{2l}(\nabla\mathbf{Q})]$ profile as a function of $\tilde{L}_3$ with the same parametric conditions of Fig. 10. The dots correspond to PR and the curve to the PP texture. The dramatic change of long-range energy at $\tilde{L}_3=-1.2$ corresponds to the texture transition point due to splay-bend elastic anisotropy. The minimum long-range energy happens when $\tilde{L}_3$ is close to 0.

computed. Lower temperature and thicker fibers tend to select the planar polar texture and higher temperature and thin fibers tend to promote the emergence of the planar radial texture, in agreement with Ref. [9]. The influence of elastic anisotropy to the fiber texture formation is thoroughly discussed. It is found that splay-bend anisotropy influences the fiber texture much more than the twist term. Splay (bend) avoidance leads to the planar radial (polar) texture. The importance of splay-bend anisotropy is completely explained by the Frank elastic theory. The results presented in this paper contribute towards a better understanding of the principles that control the cross-section texture selection during the melt spinning of mesophase carbon.

ACKNOWLEDGMENT

This grant is supported by a grant from the Donors of The Petroleum Research Fund (PRF) administered by the American Chemical Society.

[1] J. J. McHugh, Ph.D thesis, Clemson University, 1994.
[2] R. H. Hurt and Z. Y. Chen, Phys. Today **53** (3), 39 (2000).
[3] L. H. Peebles Jr., *Carbon Fibers-Formation, Structure, and Properties* (CRC, Boca Raton, 1995).
[4] P. G. de Gennes and J. Prost, *The Physics of Liquid Crystal*, 2nd ed. (Clarendon, Oxford, 1993).
[5] K. Sokalski and T. W. Ruijgrok, Physica A **113**, 126 (1982).
[6] J. E. Zimmer and J. L. White, Adv. Liq. Cryst. **5**, 157 (1983).
[7] N. Schopohl and T. J. Sluckin, Phys. Rev. Lett. **59**, 2582 (1987).
[8] G. P. Crawford and S. Zumer, *Liquid Crystals* (World Scientific, Singapore, 1995), p. 331.
[9] A. Sonnet, A. Kilian, and S. Hess, Phys. Rev. E **52**, 2702 (1995).
[10] A. P. Singh, Ph.D thesis, McGill University, 2000.
[11] L. Longa, D. Monselesan, and H. R. Trebin, Liq. Cryst. **2**, 769 (1987).
[12] D. W. Berreman and S. Meiboom, Phys. Rev. A **30**, 1955 (1984).
[13] K. Schiele and S. Trimper, Phys. Status Solidi B **118**, 267 (1983).
[14] M. Doi and B. J. Edwards, *The Theory of Polymer Dynamics* (Clarendon, Oxford, 1986).
[15] T. Tsuji and A. D. Rey, J. Non-Newtonian Fluid Mech. **73**, 127 (1997).
[16] A. N. Beris and B. J. Edwards, *Thermodynamics of Flowing Systems* (Clarendon, Oxford, 1994).
[17] M. A. Osipov and S. Hess, Mol. Phys. **78**, 1991 (1993).
[18] S. Chandrasekhar, *Liquid Crystals*, 2nd ed. (Cambridge University Press, Cambridge, 1992).
[19] J. Yan and A. D. Rey (unpublished).
[20] L. Wang and A. D. Rey, Modell. Simul. Mater. Sci. Eng. **5**, 67 (1997).